*J. Earth Syst. Sci.* (2020)129 62
https://doi.org/10.1007/s12040-019-1331-2



# Contrasting kinematics of brittle-shears within the Salem–Attur and Bhavani shear zone, south India: Tectonic implications

C Ananth[1], Subhadip Bhadra[1,*] and Abhishikta Goswami[2]

[1]*Department of Earth Sciences, Pondicherry University, Kalapet, Puducherry 605 014, India.*
[2]*Department of Applied Geology, Indian Institute of Technology, Dhanbad 826 004, India.*
**Corresponding author. e-mail: sbbh_78@yahoo.com*

MS received 8 March 2019; revised 22 October 2019; accepted 6 November 2019

We document kinematics and rheological behaviour of brittle shears (∼50 cm wide) postdating solid-state tectonic fabric in the Salem–Attur (SASZ) and Bhavani (BSZ) shear zone that constitute a Paleoproterozoic (∼2500 Ma) suture juxtaposing disparate granulite blocks in south India. We constrain brittle deformation mechanisms from established relationship between changing orientation of deflected strain marker (quartz vein) and foliation within the shear band with respect to their orientation outside the shear band. Quartz c-axis orientation in charnockite (host lithology) and phyllonite (reworked charnockite) from the SASZ show presence of mixed basal ⟨a⟩ (low-T) and prism ⟨a⟩ (high-T) slip, and single basal ⟨a⟩ slip mechanism, respectively. This suggests considerable cooling of the granulite block prior to the onset of brittle shearing. Distribution of strain parameters – effective shear strain ($\Gamma$), shear strain ($\gamma$), stretch $K_2$ along intermediate strain axis Y – from margin to the centre of the shear band, show peaked distribution with a single maximum at the shear zone centre. This implies rheological-weakening/strain-softening induced localizing shear zone character. Kinematically heterogeneous strain distribution during brittle shearing varies from transpression dominated for the BSZ to transpression-to-transtension switchover for the SASZ. Demonstrably, contrasting cooling-exhumation, hitherto unexplored, characterizes post-accretionary tectonics along the paleo-suture zone.

**Keywords.** Strain marker; rheology; EBSD analysis; Salem–Attur shear zone; Southern Granulite Terrain.

## 1. Introduction

The Southern Granulite Terrain (SGT), comprising the southern part of the Indian peninsula (figure 1), represents a hot orogen (Beaumont *et al.* 2006) with a prolonged accretionary tectonic evolution spanning Neoarchean/Paleoproterozoic to Neoproterozoic/early Cambrain (Santosh *et al.* 2009; Bhadra and Nasipuri 2017; Behera *et al.* 2019 and references therein). In the northern part of the SGT, roughly east–west trending Moyar (MSZ)–Bhavani (BSZ) and Salem–Attur (SASZ) shear zones are considered to demarcate a Paleoproterozoic suture zone along which granulites of Nilgiri Hills and Salem Block were accreted with southern part of the western Dharwar craton (figure 1). Barring few studies (Satheeshkumar and Prasannakumar 2009; Pratheesh *et al.* 2013; Prasannakumar and McCaig

Supplementary materials pertaining to this article are available on the Journal of Earth Science Website (http://www.ias.ac.in/Journals/Journal_of_Earth_System_Science).

Published online: 29 January 2020

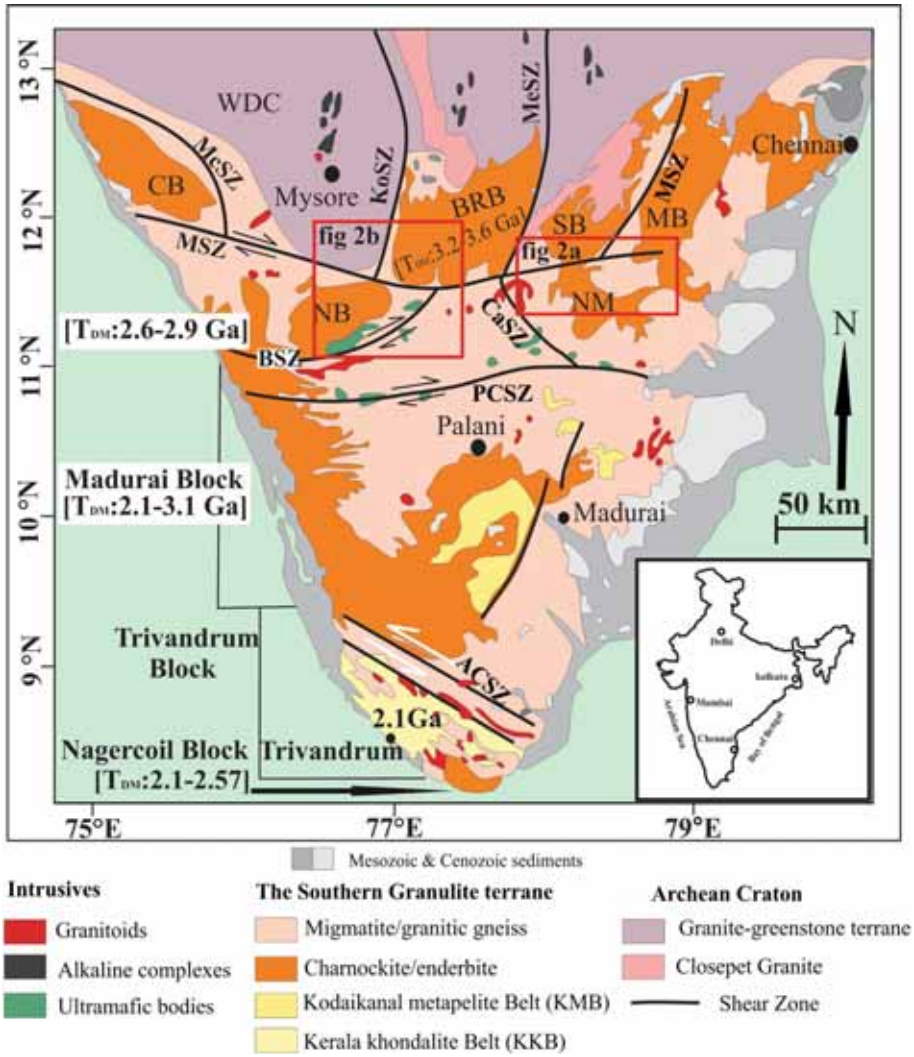


Figure 1. Tectonostratigraphic and lithological map of the southern India (modified after Ratheesh-Kumar et al. 2016; Santosh and Sajeev 2006). ACSZ: Achankovil shear zone, BRB: Biligiri Rangan Block, BSZ: Bhavani shear zone, CaSZ: Cauvery shear zone, CB: Coorg Block, KoSZ: Kollegal shear zone, MB: Madras Block, McSZ: Mercara shear zone, MeSZ: Mettur shear zone, MSZ: Moyar shear zone, NB: Nilgiri Block, NM: Namakkal Block, NSZ: Nallamalai shear zone, PCSZ: Palghat–Cauvery shear zone, SB: Shevroy Block, WDC: Western Dharwar Craton.

2016; Behera *et al.* 2019), nature, age of reactivation and cooling–exhumation history post-dating Neoarchean/Paleoproterozoic accretionary event along this 200 km long accretionary belt is still poorly constrained. This is particularly intriguing since partial-melting and metamorphic-reaction induced rheological changes during and following peak tectonic and thermal perturbation have significant bearing on the spatio-temporal evolution of hot orogens (Faccenda *et al.* 2008; Sorcar *et al.* 2014) with complex relationship between cooling and exhumation (Sorcar *et al.* 2014).

We recognize several key issues. (a) Nature and kinematics of structural grains post-dating peak orogenic stage, (b) rate of cooling along the entire length of the orogen and its relation with petrologically-constrained retrograde $P$–$T$ path, (c) rate of exhumation and its relation with cooling rate, and (d) timeframe of post-tectonic evolution constrained by suitable dating technique – that are pivotal for a holistic understanding of crustal dynamical processes following Paleoproterozoic accretion along the northern margin of the SGT. In a recent study, Behera *et al.* (2019) constrained the timing of different tectonic reworking stages within the Salem Block, in general, and the SASZ, in particular. However, information culled from literature revealed that there is complete dearth of information on the ductile to brittle transition stage, which is pervasive along the entire belt and marks the last tectonic reworking event, i.e., final cooling/exhumation stage of the orogen.

To fill these lacunae, an attempt has been made in the study to understand the kinematics and rheological behaviour of brittle shears within the SASZ and BSZ. The study focuses on kinematic analyses of deflected markers and foliation across the brittle shears in conjugation with an integrated filed structural and petrofrabric (selected thin section scale) analyses.

## 2. Geological setting

The BSZ and SASZ, with dextral sense of movement (Nair *et al.* 1981; Naha and Srinivasan 1996; D'Cruz *et al.* 2000; Chetty *et al.* 2003; Jain *et al.* 2003; Mukhopadhyay *et al.* 2003), separate Dharwar craton in the north from respectively the granulites of Nilgiri Block and Salem Block to the south. Charnockite, comprising felsic to mafic and garnet-bearing to non-garnetiferous varieties, is the dominant lithology within the granulite blocks. Geochronological studies on charnockites reveal a Mesoarchean (ca. 2800 Ma) crystallization age and widespread granulite facies metamorphism at ca. 2500 Ma (Friend and Nutman 1991; Peucat *et al.* 1993; Bartlett *et al.* 1998; Bhaskar Rao *et al.* 2003; Ghosh *et al.* 2004). Structural analyses suggest poly-phase deformation (Nair *et al.* 1981; Prasannakumar and Lloyd 2007; Biswal *et al.* 2010; Prasannakumar and Lloyd 2010) within the granulites, with SASZ as the eastern extension of the MBSZ (Drury *et al.* 1984; Chetty 1996; Raith *et al.* 1999; Bhadra 2000; Ramakrishnan 2003; Jain *et al.* 2003). These two shear zones together constitute an approximately 200 km long paleo-suture zone (figure 1). The dominant lithology in and across the SASZ is charnockite (figure 2a) whereas that across the BSZ is quartzo-feldspathic gneiss (figure 2b). Subordinate lithologies such as hornblende–biotite gneiss and phyllonite in Salem area represent retrograde charnockite (Biswal *et al.* 2010). Retrogression of charnockite to garnet-bearing quartzo-feldspathic gneiss is also reported from the Moyar shear zone (Bhadra and Nasipuri 2017), a contemporary to both BSZ and SASZ. High grade supracrustals, mafic to ultra-mafic granulites, banded magnetite quartzite constitute minor lithologies in both the BSZ and SASZ.

## 3. Mesoscopic fabric development in the shear zones

The BSZ and SASZ witnessed poly-phase deformation (Prasannakumar and Lloyd 2007; Satheeshkumar and Prasannakumar 2009; Prasannakumar and McCaig 2016; Sundaralingam *et al.* 2017; Behera *et al.* 2019). Thrusting of Namakkal Granulite Block onto the Salem Granulite Block for the SASZ and Nilgiri Granulite Block onto the southern part of the Dharwar craton for the BSZ (figures 1, 2) marks the peak-orogenic/accretionary stage.

### 3.1 *Mesoscopic fabric and fabric attitude in the SASZ*

A gneissic foliation ($S_1$) represents the penetrative fabric on mesoscopic scale (figure 3). Folding on $S_1$ is conspicuous in relatively low strain domains (figure 3a, h). Variation in strain intensity, even on outcrop-scale, is manifested by development of discrete shear band (figure 3b, g) to mylonite zone (figure 3c) with increasing strain intensity. While a distinct mylonitic foliation characterizes the high strain zone (figure 3c), transposition of $S_1$ along shear band (figure 3b) defines shear foliation in discrete shear bands. Transposed-$S_1$ fabric in shear band and mylonitic fabric mark the second fabric-forming event in both the shear zones. Therefore, the planar fabric related to this event is referred here as $S_M$ (figure 3a–d, g). As documented by Bhadra and Nasipuri (2017), $S_M$ is axial planar to the fold on early $S_1$. In the SASZ, localized fluid-ingress led to the retrogression and phyllonitization of charnockite granulite (Bhadra 2000) concomitant to the development of the shear zone. Gradational contact relationship between phyllonite bands (figure 3d) with charnockite host attests to this localized retrogression phenomenon. Phyllonitic foliation is referred as $S_P$. Tight to gentle folding on $S_M$ (figure 3f) and crenulations on $S_P$ (figure 3e) attest to later folding event. $S_M$ and $S_P$ are contemporaneous (Biswal *et al.* 2010). Axial planar fabric corresponding to the fold on $S_M$ and $S_P$ is not conspicuous. Localized brittle shear band (few tens of cm wide, figure 3g) deflects the $S_M$ solid-state fabric. Based on integrated structural and geochronological studies, Behera *et al.* (2019) recognised four deformation events, $D_1$–$D_4$, in the Salem Block. $S_M$ and $S_P$ fabric, documented above, correspond with the 2.0 Ga $D_3$ deformation event. Age of $D_4$ strike-slip shearing and pseudotachylite emplacement, possibly coinciding with $S_b$ (discussed later), within the SASZ is constrained at 1.9 Ga (Behera *et al.* 2019). Deflection of $S_1$ and pre-existing quartz veins/mafic layers across the $S_b$ is also ubiquitous in both the shear zones.

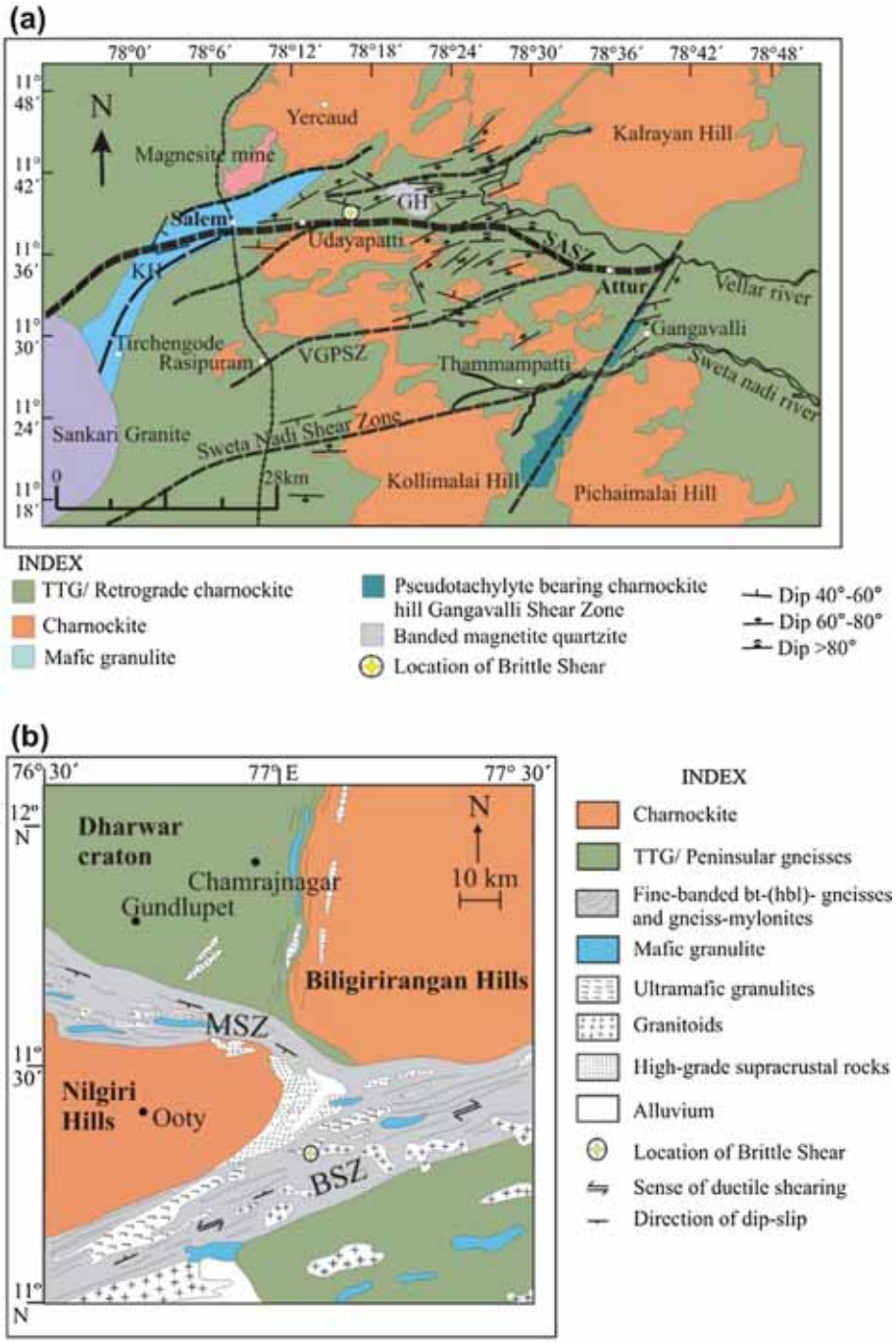


Figure 2. Detailed lithological and structural map of the study area from Salem Granulite Block (**a**) and Nilgiri Granulite Block (**b**) after Biswal *et al.* (2010) and Meißner *et al.* (2002). BSZ: Bhavani shear zone, GH: Godumalai Hill, KH: Kanjimalai Hill, MSZ: Moyar shear zone, SASZ: Salem Attur shear zone, VGPSZ: Vembagoundam Pudur shear zone.

Distribution of poles to the gneissic foliation ($S_1$) in charnockite and QFG describes three point-maxima corresponding with the limbs and hinge of fold on the gneissic layering (figure 4a). Oppositely dipping limbs vary in steepness, which suggests an asymmetric nature of the fold (figure 4a). Mean orientation of $S_1$ lies at 089°/72°N. Distribution of pole to the shear foliation ($S_M$) in shear bands within charnockite (figure 3b, c) and mylonitized charnockite (figure 3c) describes two point-maxima (figure 4b). Mean $S_M$ lies at 108°/84°S (figure 4b). The above pole distribution pattern possibly suggests a phase of tight asymmetric folding on $S_M$. Distribution of pole to the phyllonitic foliation defines a single point maximum, with mean attitude of 083°/66°N (figure 4c). Distribution of pole to the foliation reflects slight mismatch in orientation between $S_M$ (figure 4b) and $S_P$ (figure 4c).

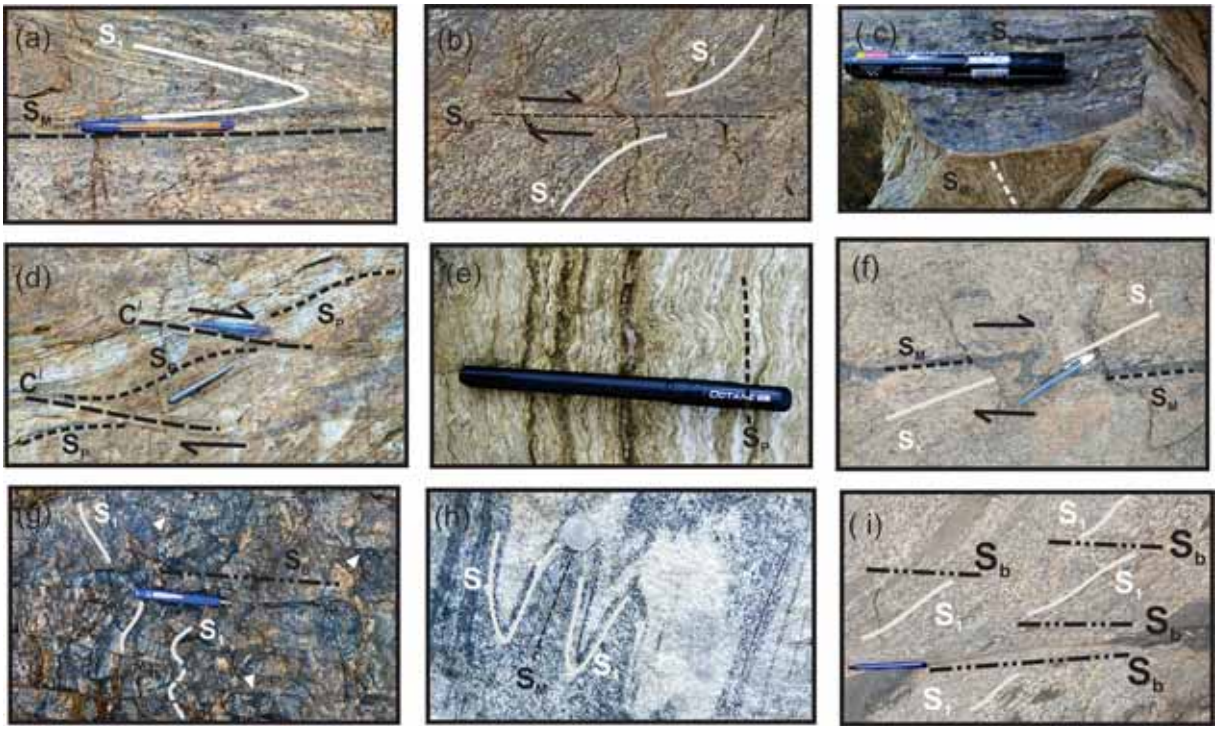


Figure 3. Field photograph from the SASZ (**a–g**) and BSZ (**h**, **i**). (**a**) Folded early gneissic ($S_1$) fabric and mylonitic ($S_M$) fabric. (**b**) $S_M$ as discrete shear band transposing the $S_1$ fabric in relative low strain zone. (**c**) Penetrative $S_M$ fabric with down dip starching lineation at high strain zone. (**d**) $S_P$ phyllontic fabric with C′ shear band. (**e**) Crenulation on $S_P$ fabric within the phyllonite band. (**f**) Tight asymmetric folding, suggesting dextral sense of hinge rotation, on $S_M$ mylonitic fabric. (**g**) Late brittle shears $S_b$ cross-cutting $S_1$ fabric. Note, segregation of pseudotachylite (marked by arrow) along $S_b$. (**h**) Folded early gneissic ($S_1$) fabric and axial planar mylonitic ($S_M$) fabric. (**i**) Penetrative $S_1$ and cross-cutting brittle shears bands $S_b$. Note, deflection of foliation and mafic enclaves by $S_b$ and absence of any pseudotachylite along $S_b$. Marker length 14 cm.

Considering overall similarity in intensity of shear fabric, presence of S–C structure (figure 3d) and sense of shearing along $S_M$ (figure 3f) and $S_P$ (figure 3d), slightly discordant attitude between $S_M$ and $S_P$ can possibly be explained by the presence of late stage C′ shear band (figure 3d) in phyllonite compared to its absence in charnockite mylonite. Structural evolution of the SASZ affirms two distinct tectonic episodes. $S_1$ and $S_M$, $S_P$ define the pre- to syn-thrusting fabric-forming event, whereas brittle shear band ($S_b$) defines the post-thrusting event. Transition from a dominantly ductile deformation ($S_1$, $S_M$ and $S_P$) to brittle deformation regime, expectedly, coincides with cooling/exhumation of the orogen.

### 3.2 *Mesoscopic fabric and fabric attitude in the Bhavani shear zone*

Bhadra and Nasipuri (2017) documented in detail the mesoscopic fabric development along the BSZ. A mylonitic foliation ($S_M$, figure 3h), varying in intensity from proto- to ultra-mylonite, dominates the planar fabric in the rock. As a result, distribution of poles to the foliation describes a point maximum (figure 4a in Bhadra and Nasipuri 2017), with mean foliation attitude at 055°/76°NW. A strong down dip lineation is present on the foliation plane. At relatively low strain domain, early gneissic fabric ($S_1$) describes tight asymmetric fold (figure 3h) with an axial planar shear foliation ($S_M$). Late brittle shear band (figure 3i) deflecting $S_M$ marks the last deformation event in the BSZ. However, compared to the SASZ, brittle shear bands are slightly more pervasive in the BSZ.

## 4. Methodology

### 4.1 *Rationale and analytical parameters for strain analysis*

Rotation of markers such as dike, quartz/calcite veins and foliation within the shear zone acts as suitable proxy to trace the strain history, rheological evolution and dynamics of the shear zone (Ramsay 1980; Fossen and Tikoff 1993; Vitale and Mazzoli 2008, 2009, 2016). We used $\theta'$–$\Gamma$ method of Vitale and Mazzoli (2010) to analyze the strain

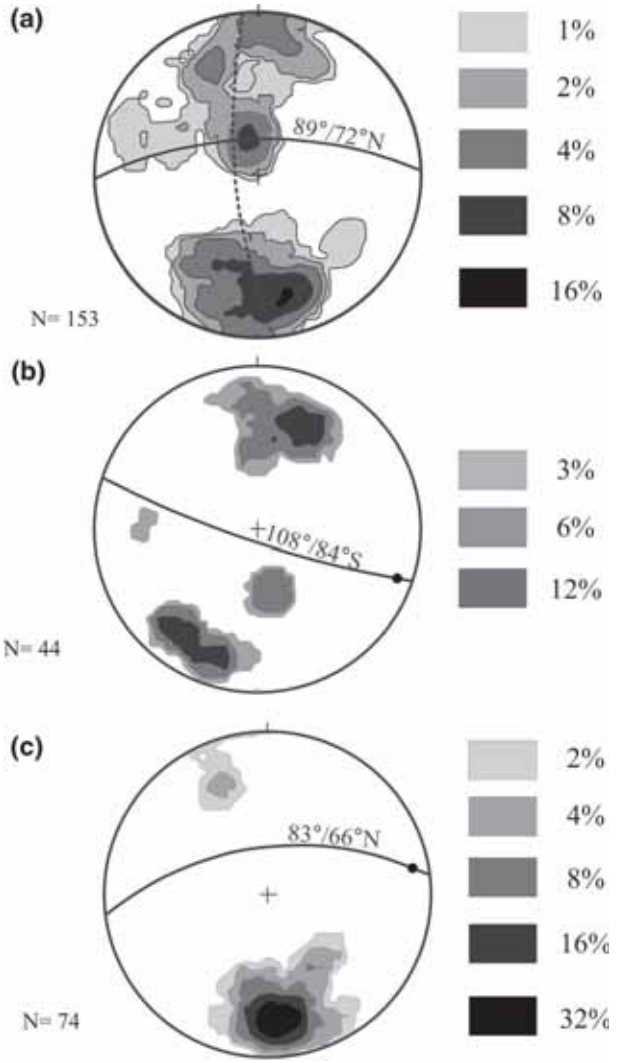


Figure 4. Stereographic projection for (**a**) gneissic foliation ($S_1$), (**b**) mylonitic foliation ($S_M$) and (**c**) phyllonitic foliation ($S_P$) from the SASZ. Orientation of $\beta$-axis corresponding to the fold on $S_M$ and $S_P$ are indicated by dots. Mean orientation is shown by solid line. N refers to number of data. Contour density given for reference.

history corresponding to development of brittle shears within the BSZ and SASZ.

Orientation of foliation and marker (dyke/vein) with respect to the intersected shear zone, defined respectively by $\theta$ and $\alpha$ (figure 5a) forms the basis of the strain analysis study. Three mutually perpendicular axes $X_1$, $X_2$ and $X_3$, define the shear zone reference frame with '$X_1$-axis' parallel to shear direction and '$X_1X_3$ plane' parallel to the shear zone (figure 5b). On the basis of the following observations, (a) brittle shears are restricted to isolated bands of width varying in few cm (SASZ: 4–5 cm, BSZ: 26 cm), implying localized pure shear component, (b) sub-vertical attitude of shear plane and foliation in both the shear zone corresponding well with the modelled reference frame (figure 5b) and (c) abundance of original (pre-brittle shearing) anhydrous mineral assemblage over incipiently developed late hydrous mineral phases, possibly suggesting constant volume deformation – we adopted the equation of strain matrix (Fossen and Tikoff 1993) where vertical stretching will result from simple shear on the '$X_1X_2$' plane and synchronous pure shear on the '$X_2X_3$' plane (figure 5b). In parameterized form this corresponds with $k_1 = 1$ and $k_3 = k_2^{-1}$ (Vitale and Mazzoli 2010), where $k_1$, $k_2$ and $k_3$ are stretches along the X, Y and Z principal strain axes, respectively. Strain parameters (discussed below) were constrained using the following basic equations (Fossen and Tikoff 1993; Tikoff and Fossen 1993; Vitale and Mazzoli 2008, 2009, 2016) pertinent to the considered strain matrix.

$$\Gamma = \cot \alpha' - \cot \alpha, \tag{1}$$

where, $\Gamma$ is effective shear strain, and $\alpha$ and $\alpha'$ denote the angle between the marker and shear plane in the undeformed host and within the shear zone. $\theta'$–$\Gamma$ grid of Vitale and Mazzoli (2010) is constructed by varying the values of $k_2$ and $\gamma$ following the equations (Fossen and Tikoff 1993; Tikoff and Fossen 1993)

$$\Gamma = \frac{\gamma(k_1 - k_2)}{\ln(k_1/k_2)}, \tag{2}$$

$$\tan \theta' = \frac{\lambda_{\max} - \Gamma^2 - 1}{k_2 \Gamma}, \tag{3}$$

where $\lambda_{\max}$, maximum quadratic elongation of the bulk strain ellipsoid, is the maximum among the three eigenvalues of the strain matrix. Quadratic elongations along X, Y and Z axes of the strain ellipsoid, i.e., $\lambda_1$, $\lambda_2$ and $\lambda_3$ are defined as:

$$\lambda_1 = \left\{\frac{1}{2}\left(\Gamma^2 + 1 + k_2^2 + \sqrt{-4k_2^2 + \left(\Gamma^2 + 1 + k_2^2\right)^2}\right)\right\}, \tag{4}$$

$$\lambda_2 = \left\{k_2^2\right\}, \tag{5}$$

$$\lambda_3 = \left\{\frac{1}{2}\left(\Gamma^2 + 1 + k_2^2 - \sqrt{-4k_2^2 + \left(\Gamma^2 + 1 + k_2^2\right)^2}\right)\right\}, \tag{6}$$

$k_2$ is defined as (Vitale and Mazzoli 2016),

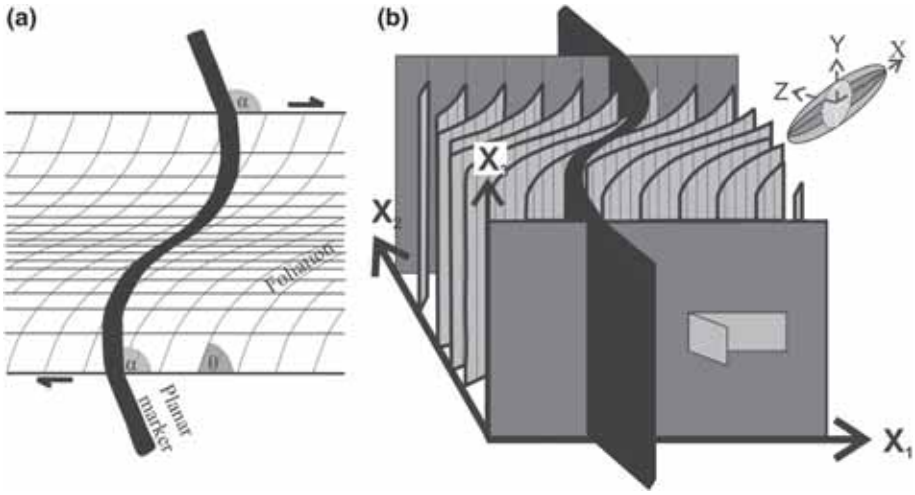


Figure 5. (**a**) Cartoon showing the parametric sectional view (plane '$X_1X_2$' in (b): parallel to the slip vector) of deflected marker within a shear zone and the pictorial definition three angles required for strain analysis (see text for reference) after Vitale and Mazzoli (2016). (**b**) A 3D view, with $X_1$, $X_2$, $X_3$ reference axes, of the shear zone depicting geometric relationship between foliation plane (XY plane of the strain ellipsoid) and the deflected marker (thick black line). Note a strain ellipsoid with X, Y and Z principal strain axes is given for reference.

$$k_2 = \frac{\Gamma(\tan\theta')^2 - \Gamma - \sqrt{\Gamma^2(\tan\theta')^4 + 2\Gamma^2(\tan\theta')^2 + \Gamma^2 + 4(\tan\theta')^2}}{2\tan\theta'}. \quad (7)$$

Vorticity ($W_k$) is expressed as,

$$W_k = \cos\left\{\arctan\left[\frac{2\ln k_2}{\gamma}\right]\right\}. \quad (8)$$

Incremental strain parameters, given below are calculated using procedure described in Vitale and Mazzoli (2016),

$$k_1^{incr} = \frac{\left(k_1^{fin}\right)_i}{\left(k_1^{fin}\right)_{i-1}}, \quad k_2^{incr} = \frac{\left(k_2^{fin}\right)_i}{\left(k_2^{fin}\right)_{i-1}}, \quad k_3^{incr} = \frac{\left(k_3^{fin}\right)_i}{\left(k_3^{fin}\right)_{i-1}}, \quad (9)$$

where, 'incr' and 'fin' refer to incremental and finite state respectively, and '*i*' refers to the *i*th layer (figures 6, 7).

### 4.2 *Fabric–strain marker relationship*

#### 4.2.1 *The SASZ*

Four to five cm wide late brittle shear band ($S_b$) deflects the strain marker, a 1.13 cm wide quartz vein, and the $S_1$ foliation in charnockite (figure 6). Near asymptotic nature of strain-marker and foliation with the general trend of the $S_b$ determines the central segment of the shear band (figure 6b, c). The entire width of the shear band is divided into 11 layers, A1–A11 (figure 6c), with layer spacing varying logarithmically to account for heterogeneous strain distribution. $\alpha'$ and $\theta'$ values across the brittle shear band are summarized in table 1.

#### 4.2.2 *The BSZ*

A 26 cm wide brittle shear band deflects the strain marker, 3.3 cm wide quartz vein (figure 7a, b). The entire width (26 cm) of the shear band is divided into 21 layers, 10 layers B1–B10 on the upper half (B-series) and 11 layers C1–C11 (figure 7c) on the lower half (C-series). 10th layer (B10) on upper half and 11th (C11) on the lower half coincide with central part and 1st layer (B1 and C1) coincides with boundary of the shear band. Values of $\alpha'$ and $\theta'$ are summarized in table 2. Due to broad similarity in their strain history, strain analytical results for the upper half is discussed in detail in the following section (section 5.3).

### 4.3 *Electron backscatter diffraction (EBSD) analysis*

A Carl Zeiss Auriga Compact FEG–SEM (scanning electron microscope) instrument fitted with NordlysMax2 EBSD detector (Oxford instruments, UK) at the Central Research Facility (CRF) IIT Kharagpur, India was used for EBSD analyses.

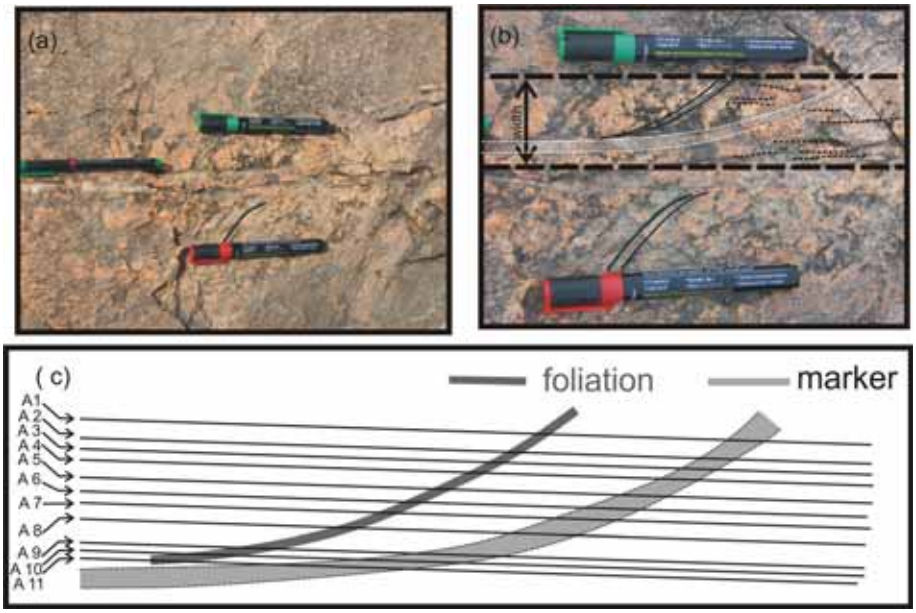


Figure 6. (**a**, **b**) Field photograph and (**c**) cartoon of brittle shear band from the SASZ. Marker and the brittle shears are indicated by white and black dotted lines, respectively. Note the central part and width of the shear band are demarcated using the deflected marker in (**b**), and logarithmic subdivision of the shear band into 11 layer segments (A1–A11) in (**c**). See text for reference. Marker length 14 cm.

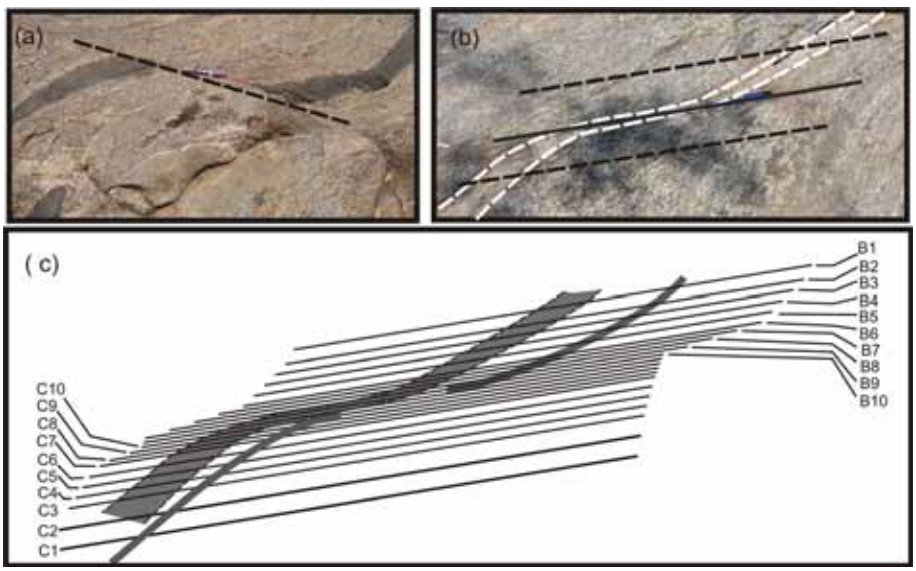


Figure 7. (**a**, **b**) Field photograph and (**c**) cartoon of brittle shear band from the BSZ. Marker is indicated by white dotted line. Note the central part and width of the shear band are demarcated using the deflected marker in (**b**), and logarithmic subdivision of the shear band into 10 layer segments (B1–B10 and C1–C10) on either side of the central part in (**c**). See text for reference. Marker length 14 cm.

EBSD data acquisition and post-processing were carried out using AZtec software and HKL Channel 5 software, respectively. Operating conditions for EBSD analysis are available in Sawant *et al.* (2017). For the BSZ, we culled the information of EBSD analytical results documented by Prasannakumar and Lloyd (2007).

## 5. Results

### 5.1 *Electron backscatter diffraction (EBSD) petrofabric analysis of quartz*

The purpose of EBSD analyses for determining c-axis orientation of quartz grains in charnockite

Table 1. *Measured orientation parameters (figure 5) and calculated strain parameters for brittle shear band within the SASZ.*

| Layer no. | $\alpha'$ | $\theta'$ | $\Gamma$ | $K_2$ | $\gamma$ | $W_K$ | $R_{XZ}$ |
|---|---|---|---|---|---|---|---|
| A1 | 39.84 | 36.83 | 0.26 | 0.96 | 0.27 | 0.96 | 1.31 |
| A2 | 36.76 | 30.17 | 0.40 | 0.87 | 0.43 | 0.85 | 1.57 |
| A3 | 35.50 | 28.67 | 0.47 | 0.84 | 0.51 | 0.83 | 1.70 |
| A4 | 34.44 | 26.38 | 0.52 | 0.80 | 0.59 | 0.79 | 1.86 |
| A5 | 32.27 | 20.77 | 0.65 | 0.67 | 0.79 | 0.70 | 2.38 |
| A6 | 30.46 | 19.64 | 0.77 | 0.63 | 0.96 | 0.72 | 2.78 |
| A7 | 25.92 | 18.07 | 1.12 | 0.61 | 1.42 | 0.82 | 4.06 |
| A8 | 19.04 | 16.63 | 1.96 | 0.72 | 2.30 | 0.96 | 7.30 |
| A9 | 11.89 | 11.84 | 3.81 | 0.85 | 4.13 | 1.00 | 19.05 |
| A10 | 8.32 | 8.98 | 5.91 | 0.96 | 6.03 | 1.00 | 38.31 |
| A11 | 6.08 | 7.22 | 8.45 | 1.09 | 8.11 | 1.00 | 67.77 |
| | $\alpha = 46.96$ and $\theta = 44.48$ | | | | | | |

See text for discussion.

Table 2. *Measured orientation parameters (figure 6) and calculated strain parameters for brittle shear band within the BSZ.*

| Layer no. | $\alpha'$ | $\theta'$ | $\Gamma$ | $K_2$ | $\gamma$ | $W_K$ | $R_{XZ}$ |
|---|---|---|---|---|---|---|---|
| B1 | 32.18 | 29.29 | 0.29 | 0.88 | 0.31 | 0.77 | 1.39 |
| B2 | 29.70 | 26.53 | 0.45 | 0.81 | 0.50 | 0.76 | 1.71 |
| B3 | 27.88 | 25.56 | 0.59 | 0.78 | 0.66 | 0.80 | 2.01 |
| B4 | 26.32 | 22.67 | 0.72 | 0.71 | 0.85 | 0.78 | 2.43 |
| B5 | 22.02 | 20.81 | 1.17 | 0.71 | 1.38 | 0.90 | 3.79 |
| B6 | 20.14 | 19.58 | 1.42 | 0.72 | 1.67 | 0.93 | 4.72 |
| B7 | 18.04 | 15.62 | 1.77 | 0.64 | 2.20 | 0.93 | 6.96 |
| B8 | 15.90 | 14.93 | 2.21 | 0.70 | 2.62 | 0.96 | 8.98 |
| B9 | 12.27 | 11.13 | 3.29 | 0.71 | 3.90 | 0.98 | 17.45 |
| B10 | 8.46 | 7.66 | 5.42 | 0.75 | 6.22 | 1.00 | 41.05 |
| | $\alpha = 37.50$ and $\theta = 32.35$ | | | | | | |

See text for discussion.

granulite (having mm-wide shear band ($S_M$) and pseudotachylite vein) and phyllonite band (retrogressed charnockite) from the SASZ was two-fold (a) to understand the kinematic of the shear zone, i.e., dextral *vs.* sinistral shear sense for correlating late stage fabrics, i.e., $S_M$ and $S_p$ in charnockite and (b) to constrain deformation temperature corresponding to phyllonitization, especially in absence of suitable mineralogy for conventional mineral geothermometry.

Stereographic projections of c-axis orientation for quartz grains in pseudotachylite-bearing charnockite, having mm to cm wide shear band, and phyllonite are depicted in figure 8. c-axis of quartz grains from host charnockite defines two maxima, close to the 'Z' and close to the 'Y' axis (figure 8a). The phyllonite, on the contrary, is characterized by a single c-axis maximum close to the 'Z' axis (figure 8b). Rotation of the monoclinic c-axis girdle corresponds with a dextral sense of shearing in both the samples (figure 8) that matches with mesoscopic shear sense deduced from suitable markers (figure 3). c-axis cluster close to Y-axis suggests operation of prism ⟨a⟩ slip, whereas that close to Z-axis suggests basal ⟨a⟩ slip mechanisms (Neumann 2000; Hunter *et al.* 2018 and references therein). Prism ⟨a⟩ and basal ⟨a⟩ slips are indicative of respectively moderate-to-high (>500°C) and low (<400°C) temperature deformation condition (Neumann 2000; Hunter *et al.* 2018 and references therein). The EBSD results, therefore, affirm a low temperature reworking of the host charnockite gneisses that seemingly qualifies to the condition of $S_M$ fabric in charnockite.

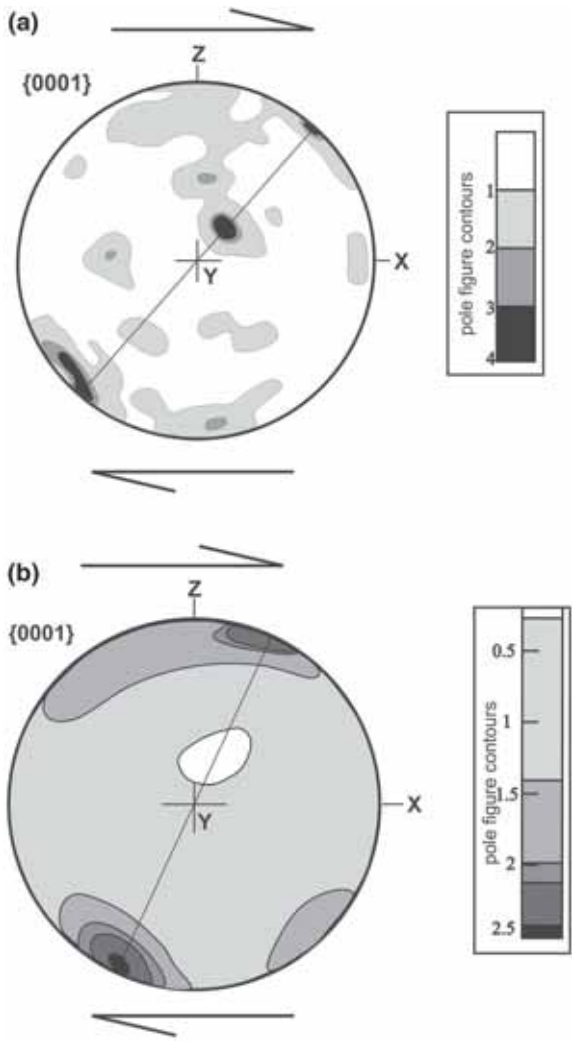


Figure 8. EBSD c-axis preferred orientation of quartz in (**a**) charnockite granulite and (**b**) phyllonite from the SASZ. Note the monoclinic nature of the c-axis girdle suggesting simple shear deformation with dextral shear sense. Note two maximum close to Y, i.e., prism ⟨a⟩ slip and along periphery clockwise from Z, i.e., basal ⟨a⟩ slip in (**a**) and one maximum, basal ⟨a⟩, in (**b**).

Importantly the condition of low-T reworking in gneisses closely matches with deformation temperature condition prevailed during phyllonitisation. A comparison with the mesoscopic fabric elements, discussed in section 3, therefore, suggests coeval nature of $S_M$ and $S_P$. Deformation at low temperature, documented above, during $S_M/S_P$ fabric formation establishes a stage of exhumation. Attainment of greenschist facies condition (figure 8) appears to be concordant with the formation of late brittle shears, indicating a transition in deformation behaviour from ductile to brittle. EBSD c-axis orientation of quartz, biotite and amphibole grains in the sheared quartzo-feldspathic gneiss from the Bhavani shear zone (Prasannakumar and Lloyd 2007) and syenite from the Moyar shear zone (Pratheesh *et al.* 2013) also reveal polyphase deformation history and low-T, amphibolite to greenschist facies, reactivation of Neoarchean granulites in these shear zones.

EBSD quartz c-axis orientation analyses in conjugation with the observed temporal relationship among fabric development events, collectively, validate development of brittle shear bands ($S_b$) in response to the exhumation in the respective orogen. These shear bands are therefore ideally suited for constraining post-orogenic tectonic evolution across the SASZ and BSZ.

### 5.2 *Finite and incremental strain history of brittle shears from the SASZ*

Finite shear strain ($\gamma$), finite effective shear strain ($\Gamma$) and $R_{XZ}$ ($=\lambda_1/\lambda_3$, strain ellipticity on the XZ plane of strain ellipsoid) across the chosen layers (figure 6b, c) of the shear band increase non-linearly with decreasing $\theta'$ values (figure 9a–c). $R_{XZ}$ (figure 10a) and $\gamma$ (figure 10b) across the layers show a peaked distribution pattern, with a single maximum. Incremental $R_{XZ}$ (figure 10a) and $\gamma$ (figure 10b) display a sharp increase before flattening out proximal to the central part of the shear band. Finite stretch along intermediate strain axis ($K_2$) shows non-linear distribution with an initial decrease followed by a steady increase towards the central part of the shear band (figure 10c). The above variation suggests a transition from dominantly transpression ($K_2 < 1$) to transtension ($K_2 > 1$) at the central part. Finite vorticity ($W_K$) also shows similar trend with a simple shear dominated deformation regime for the central part (figure 10d). Incremental $K_2$ shows gradual linear increase towards the central part (figure 10c). Incremental vorticity displays a non-linear increase towards the central part (figure 10d).

The finite strain history of the shear band, when viewed on a $\theta'$–$\Gamma$ space, suggests a switchover from transpression dominated deformation regime at the margin to transtension dominated one at its central part (figure 11a). Incremental strain path also reflects a transition into transtension-dominated deformation behaviour for the central part of the shear band. Further, $\gamma$–$K_2$ diagram with $W_K$-isolines (Fossen and Tikoff 1993) not only corroborates transpression-to-transtension switchover, mentioned above but also suggests a change in the orientation of the maximum stretching axis (X) with increasing vorticity, i.e., simple shear component (figure 11b). Biswal *et al.* (2010) reported stretching lineations with dominantly vertical plunge and subordinate horizontal plunge from the SASZ. Though the authors invoked fold-interference mechanism for the change in orientation of maximum stretching direction, the observed strain path (figure 10a, b) may provide a possible alternative explanation.

On logarithmic Flinn diagram (Flinn 1962; Ramsay 1967), we observed a noticeable discordance between stretch ($K_2$, figure 10c) and finite strain path (figure 11a) with the strain type (figure 11c). Finite strain values plot on a constriction type of strain ellipsoid (figure 11c) as opposed to their transpression-dominated strain history (figure 11a) and below-unity finite $K_2$ values (figure 10c). Incremental strains, on the contrary, characterize a flattening type strain. Implication for such discrepancy is discussed later.

### 5.3 *Finite and incremental strain history of brittle shears from the BSZ*

A non-linear increase in $\gamma$, $\Gamma$ and $R_{XZ}$ with decreasing $\theta'$ values is also evident across the chosen layers (figure 7b, c, supplementary figure S1) within the brittle shear band (figure 9d–f). $R_{XZ}$ (figure 10e) and $\gamma$ (figure 10f) show peaked distribution pattern, with a single maximum. Incremental $R_{XZ}$ (figure 10e) and $\gamma$ (figure 10f) display a gradual increase towards the central part of the shear band. Finite stretch along intermediate strain axis ($K_2$) remains more or less constant at values less than unity (figure 10g). Finite vorticity ($W_K$) also shows gradual increase from general shear dominated one at the margin to simple shear dominated deformation regime at the

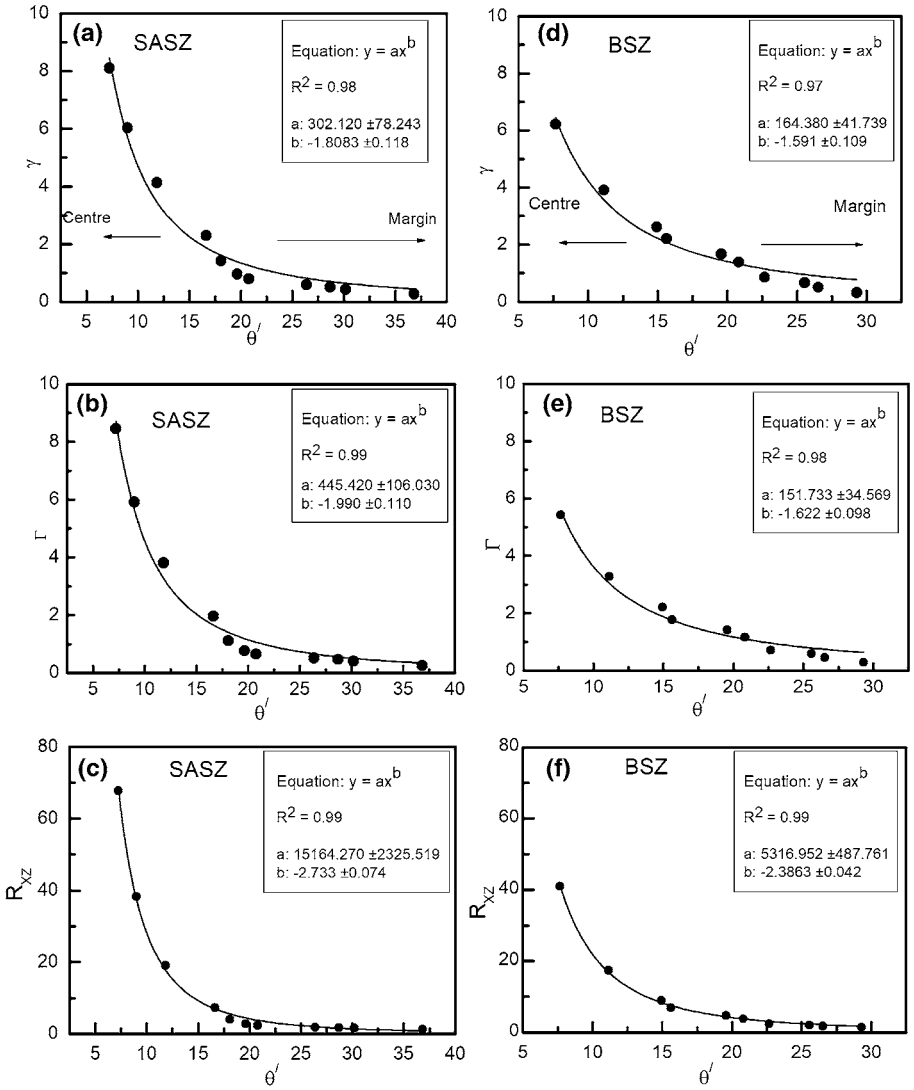


Figure 9. Variation diagram of finite shear strain $\gamma$ (**a**, **d**); finite effective shear strain $\Gamma$ (**b**, **e**) and finite strain ratio $R_{XZ}$ (**c**, **f**) *vs.* finite angle $\theta'$ for the brittle shear band (figure 6), layer A1–A11, within the SASZ and upper half of the brittle shear band (figure 7c), layer B1–B10, within the BSZ. Best-fit exponential curve and fit parameters are given for reference.

central part (figure 10h). Incremental $K_2$ progressively increases towards the central part (figure 10c) and culminates at values higher than unity. Incremental vorticity values from margin to centre almost mimics the finite vorticity path (figure 10h).

On a $\theta'$–$\Gamma$ space, the finite strain history of the shear band shows a transpression dominated deformation regime for the entire shear band (figure 12a, supplementary figure S2). Incremental strain path also reflects similar deformation behaviour (figure 12a). $\gamma$–$K_2$ plot (Fossen and Tikoff 1993) also reveals a dominantly transpressive deformation regime (figure 12b, supplementary figure S2) with vertical orientation for maximum stretching axis (X). The observation tallies with the vertical stretching lineation (Bhadra and Nasipuri 2017) on the shear fabric ($S_M$) reported from the BSZ.

Discordance, likewise the SASZ, is observed between stretch ($K_2$, figure 10g) and finite strain path (figure 12a) with the strain type (figure 12c). The results from the BSZ, as well as SASZ, suggest a component of constriction during transpression. Incremental strain path, however, fits well with the observed transpressive deformation condition.

## 6. Discussion

### 6.1 *Origin of brittle shear band: Kinematic and rheological perspective*

Localized high strain, as evidenced from $\gamma$ and $\Gamma$ maximum (figure 9a, b, d, e), at the central part

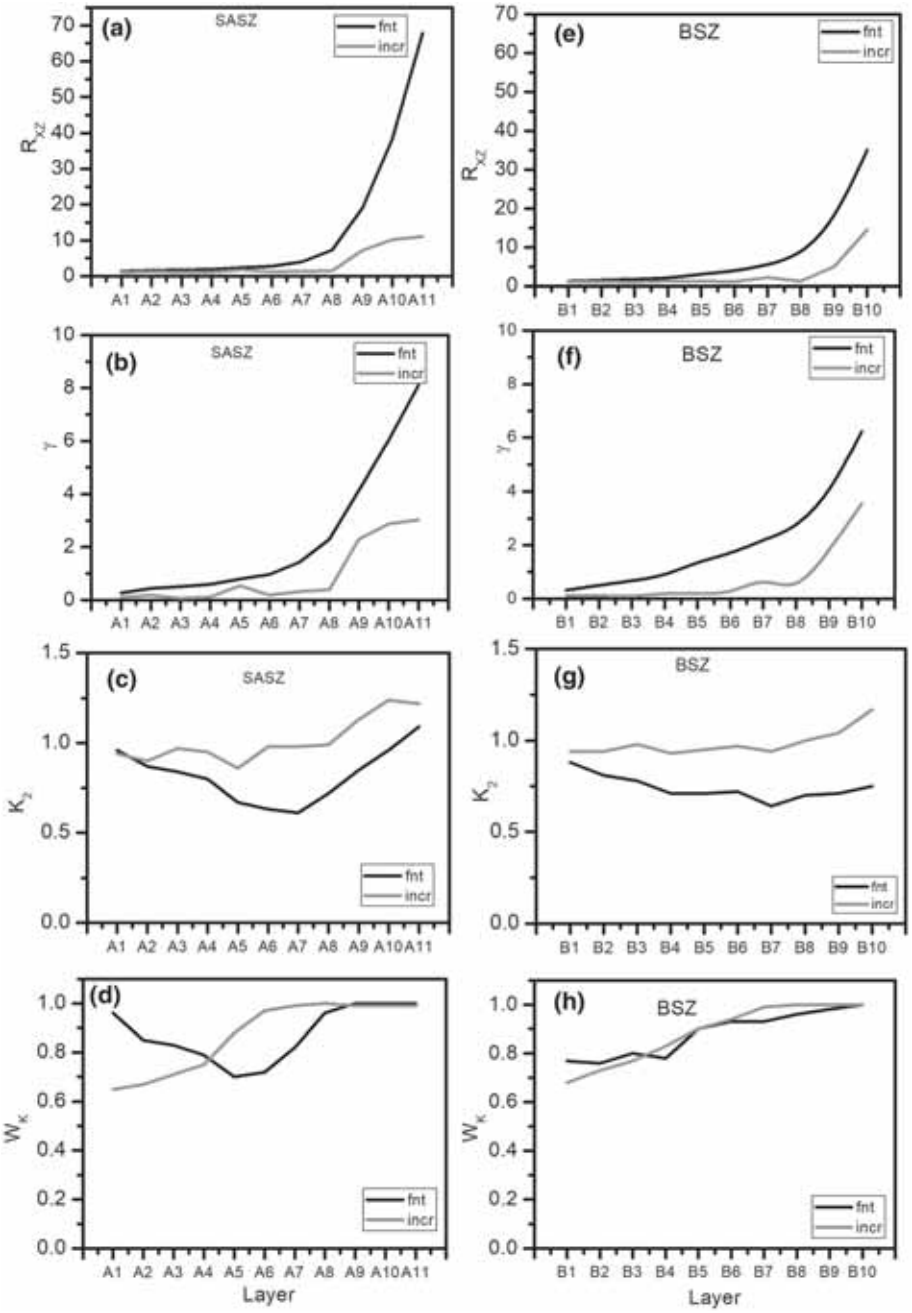


Figure 10. Variation of finite and incremental values of strain ratio $R_{XZ}$ (**a**, **e**); shear strain $\gamma$ (**b**, **f**); elongation $K_2$ (**c**, **g**) and vorticity $W_K$ (**d**, **h**) *vs.* the layers, described in figures 6 and 7, across the shear band within the SASZ and BSZ. 'fnt' and 'incr' refer to finite and incremental, respectively.

and exponential decrease of strain magnitude towards the boundary of the studied brittle shear bands within the BSZ and SASZ are commensurate with heterogeneous strain pattern that characterizes shear zone, in general.

Strain intensity, $\Gamma$ value (Vitale and Mazzoli 2010), during brittle shear band development is slightly weaker ($\Gamma < 5.42$) in the BSZ compared to the SASZ ($\Gamma \sim 8.45$). Strain ellipticity on the XZ plane ($R_{XZ}$) for brittle shearing in the SASZ ($R_{XZ} = 68$, table 1) and the BSZ ($R_{XZ} = 40$, table 2) further testifies this fact. Peaked distribution with a single maximum for strain parameters, i.e., $R_{XZ}$, $\gamma$ (figure 10a, b, e, f), suggests a rheological weakening and strain-softening mechanism during temporal evolution of the brittle shear bands. Strain softening leads to development of 'localizing shear zone' (Means 1984, 1995; Hull 1988; Horsman and Tikoff 2007). Temporal reduction in shear zone width caused by strain

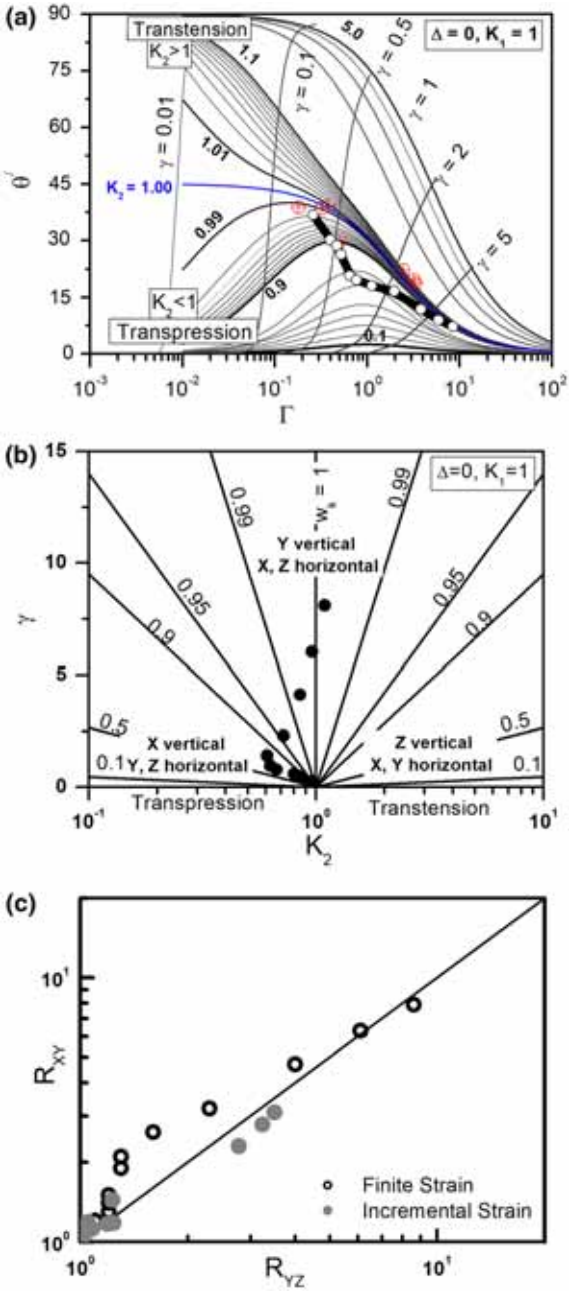


Figure 11. (**a**) $\theta'$–$\Gamma$, (**b**) $\gamma$–$K_2$ scatter diagram and (**c**) Flinn diagram showing the variation of finite and incremental strain from margin to centre of the brittle shear band, as measured across the segmented layers A1–A11 (figure 6c), from the SASZ.

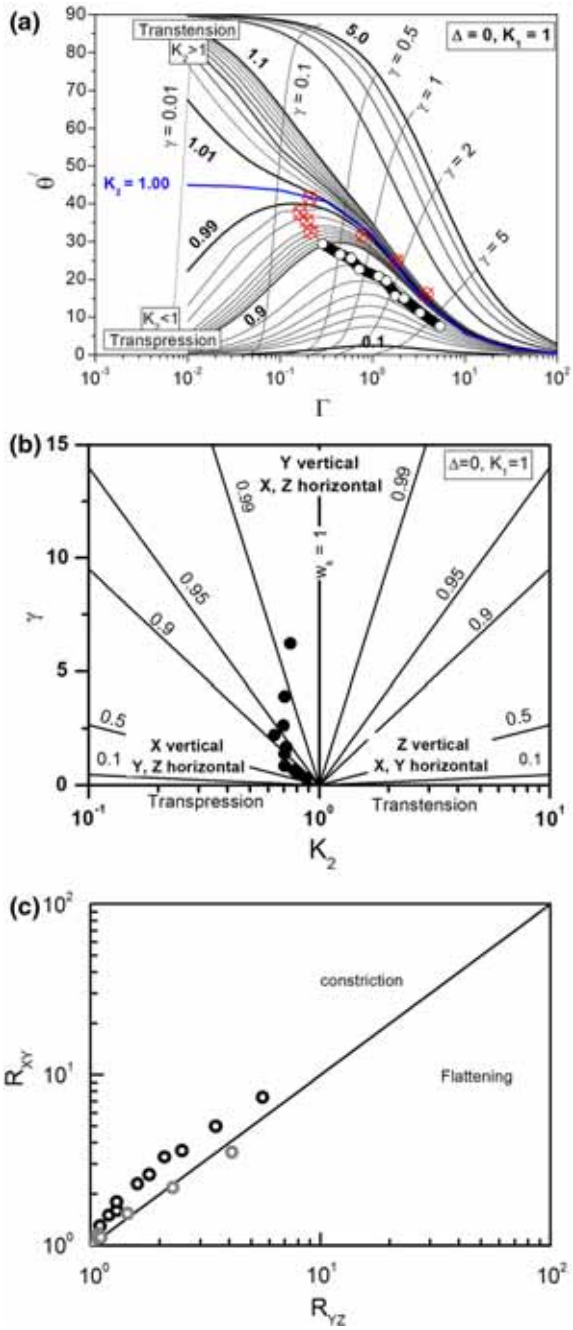


Figure 12. (**a**) $\theta'$–$\Gamma$, (**b**) $\gamma$–$K_2$ scatter diagram and (**c**) Flinn diagram showing the variation of finite and incremental strain from margin to centre of the brittle shear band, as measured across the segmented layers B1–B10 (figure 7c), from the BSZ.

localization within the inner part of shear zone compared to its margin, which becomes progressively inactive, characterizes such shear zones. In addition, non-uniform values of incremental strain parameters across the shear band manifest non-steady state deformation during temporal evolution of the brittle shear band (figure 10). In spite of above similarities, noticeable discordances exist in kinematic evolution of the SASZ and BSZ.

The nature of deformation at the central part of the shear band is dominantly transtensional for the SASZ and transpressional for the BSZ. Distinct variation (figure 10c *vs.* 10g) of stretching along intermediate strain axis ($K_2$) for shear band development in respective shear zones testifies this fact. The observed variation of $K_2$ (figure 10c) suggests a switchover of deformation mechanism from transpression-dominated ($K_2 < 1$) at the

margin to transtension dominated ($K_2 > 1$) at the centre of the shear band within the SASZ. Finite intermediate stretch ($K_2$), on the other hand, shows a near constant to slightly decreasing trend (figure 10g) towards the centre of brittle shear band within the BSZ. $K_2$ consistently remains below unity suggesting a transpression dominated deformation regime. $\theta'$–$\Gamma$ (figures 11a, 12a) and $\gamma$–$K_2$ (figures 11b, 12b) diagrams that take into account combined effect of finite shear strain, stretch, and vorticity during the temporal evolution of brittle shear bands also reveal distinctly different deformation regime for the BSZ and SASZ. Vorticity values for the brittle shears within the SASZ (figure 10d) and BSZ (figure 10h) reveal partitioning of simple shear component of deformation over pure shear in domain of high shear strain. Component of pure shear increases towards the margin in both the shear bands, characterizing a general shear dominated deformation regime. However, partitioning of simple shear and pure shear component of deformation seems to differ in these two bands. Brittle shear band hosted in the SASZ shows a divergence between finite and incremental vorticity path (figure 10d) that may possibly attest to heterogeneous strain localization across the band. On mesoscopic scale, presence of weak penetrative fabric in the host charnockite (figure 6a) seemingly manifests the localized deformation that possibly prevailed during the development of brittle shear band. Near convergent finite and incremental vorticity values (figure 10h) for shear bands in the BSZ, on the contrary, points towards homogeneous deformation that affected both the host rock and the shear band. Pervasive, penetrative foliation in the host rock (figure 7a) possibly attests to such deformation behaviour. Conformable correlation between field structural observation and strain modelling results, therefore, appear significant towards the success of strain analytical techniques, adopted in this study. In addition, following observations further strengthen the above fact.

As documented earlier, variation of intermediate stretch ($K_2$) and finite shear strain ($\gamma$), as a function of vorticity ($W_k$), suggests a switchover in orientation of maximum principal stretching direction (X-axis of bulk strain ellipsoid) from vertical to horizontal with progressively increasing vorticity in both the SASZ (figure 11b) and BSZ (figure 12b) brittle shear bands. Change in orientation of stretching lineation on mesoscopic scale, due to superposed deformation, was reported from the SASZ (Biswal *et al.* 2010), BSZ (Prasannakumar and Lloyd 2007) and MSZ (Pratheesh *et al.* 2013). Shear bands are common feature at late stage of evolution of shear zone characterized by both ductile and brittle deformation (Passchier 1984). Such an evolutionary trend, therefore, genetically links brittle shear bands with the mylonitic ($S_M$ in the SASZ and BSZ) and phyllonitic ($S_P$ in the SASZ), fabric-forming event. In this scenario, the strain analytical result, documented in this study, may provide an alternative interpretation where rotation of stretching lineation appears to be intrinsic to a single progressive deformation event. Petrofabric analytical results for charnockite and phyllonite from the SASZ (section 5.1) seem intriguing in this regard. Dextral monoclinic c-axis girdle (figure 8) in phyllonite tallies perfectly with the mesoscopic dextral shear sense (Biswal *et al.* 2010 and this study) obtained from mylonitic ($S_M$) and phyllonitic ($S_P$) fabric. In addition, EBSD c-axis orientation of quartz grains in phyllonite suggests a low temperature (basal ⟨a⟩ slip mechanism, figure 8) deformation event. This observation is in conformity with that of Biswal *et al.* (2010) and Behera *et al.* (2019) who correlated the mylonite/phyllonite fabric in the SASZ with a late low-T reworking of Neoarchean high-grade charnockite granulites. Petrofabric results (figure 8) further suggest a low-temperature reworking in Salem charnockite granulite. In the SASZ, strain-softening and localized simple shear dominated deformation during the temporal evolution of brittle shear band marks the tectonic signature of this low-T reworking event. Importantly a component of extension (figure 11b) also appears to be significant during the late stage kinematic evolution of the brittle shear band. Behera *et al.* (2019) documented two stages of brittle deformation events ($D_4$ stage), ca. 1.9 Ga strike-slip shearing and ca. 0.5 Ga normal faulting in the Salem area. Pseudotachylite emplacement broadly coincides with the $D_4$ strike-slip shearing, whereas normal faulting marks an end stage of extension. Pseudotachylite emplacement along the late brittle shear (figure 3g) and high vorticity value ($W_K$) for brittle shearing (figure 10d) tally well with the $D_4$ strike-slip brittle shearing. Correspondence between our strain analytical results and recently published works from the study area though seems promising, more precise and exhaustive studies are required to correlate the extension phase, documented in association with the origin of shear bands, with the $D_4$ normal faulting.

Owing to similarities in character (localizing shear zone character) and mechanism (strain-softening) of development of shear bands in the SASZ and BSZ, temporal evolution of the brittle shear bands arguably marks the tectonic signature of low-T reworking event in the BSZ. In contrast to its SASZ counterpart, strain analytical results from the BSZ document an entirely transpression dominated deformation regime with homogeneous strain affecting the brittle shear band and the host rock.

Interestingly, both the shear bands record a constriction type of finite strain path (figures 11c, 12c), which contradicts with widely accepted flattening-type strain character of transpression (Fossen and Tikoff 1993). However, constriction during transpression may arise from lateral escape (Dias and Rebeiro 1994) during orogenesis and compression along intermediate strain axes (Fletcher and Bartley 1994). Though establishing operation of such mechanisms is beyond the scope of this communication, the observation appears significant and warrants detailed investigation into the exhumation mechanisms along this ancient orogenic belt.

### 6.2 *Tectonic implications*

The granulite terranes of south India evolved through two major, i.e., Neoarchean and Late Neoproterozoic/early Cambrian, subduction accretionary tectonics, which manifest amalgamation of respectively granulite terranes, e.g., Nilgiri Granulite Block, Salem Granulite Block (figure 1, referred as northern granulite terrane, NGT), along the southern margin of the Dharwar craton with ca. 2.5 Ga granulite facies reworking and the NGT with the SGT (figure 1) coinciding with possible closure of paleo-Mozambique ocean during early Cambrian Gondwana assembly (Pan-African orogeny ca. 550 Ma). However, barring few geochronological records (Bhaskar Rao *et al.* 1996; Meiβner *et al.* 2002; Ghosh *et al.* 2004; Behera *et al.* 2019), there is dearth of information on the Pan-African tectonic imprints from the BSZ and SASZ, i.e., across this Neoarchean accretionary belt. In the context of tectonic complexity of the polychronous orogen, the observations of Clark *et al.* (2009), Biswal *et al.* (2010) and Sato *et al.* (2011) seem pertinent. Clark *et al.* (2009) postulated the possibility of localized Neoproterozoic reworking along discrete shear zones in the Salem area. Biswal *et al.* (2010) recognized the SASZ as a basal detachment juxtaposing the NGT and SGT. The authors considered the thrusting event to post-date Neoarchean granulite facies metamorphism. Sato *et al.* (2011) emphasized on understanding the temporal relation between formation and metamorphism of various lithologies along Moyar–Bhavani–Salem–Attur shear zone (MBSASZ, Sato *et al.* 2011) in order to recognize tectonic signatures specific to the Neoarchean and Neoproterozoic orogenic event.

Contrasting tectonic style during late stage of brittle shearing event within the BSZ and SASZ, documented here, calls for more integrated studies to understand the temporal relationship among various deformation stages, both within and across the SASZ and BSZ. In absence of such comprehensive database, petrofabric results of the present study provide some useful evidence in recognising post-Neoarchean tectonic imprint in the SASZ, in particular and along the BSZ, by analogy. Petrofabric and strain analytical results from the SASZ and BSZ unequivocally linked the transition from ductile solid–state fabric ($S_1$, $S_M/S_P$) to brittle shear fabric ($S_b$) with cooling/exhumation of the respective orogen. In case, the observed ductile to brittle transition represents a waning stage of single continuous orogenic event along the Paleoproterozoic suture zone, the relative time span of orogenic cycle bears significant clues to the rheological changes associated with the strength of lower crust during orogenesis and orogenic exhumation processes (Faccenda and Mancktelow 2010; Magni *et al.* 2013). Special relevance to the duration of ductile to brittle deformation event lies in the coexistence of mylonitic-/shear band-fabric and late brittle deformation-induced pseudotachylite formation in the SASZ (figure 3g). Jiang *et al.* (2015) from eastern Peninsular Range Batholith (PRB, California) documented that such existence (broadly coeval in PRB) represents a feedback relationship whereby pre-existing mylonite fabric localizes brittle deformation and feeds to the growth of pseudotachylite in terms of selective melting of phyllosilicate (biotite) phases defining the mylonitic fabric. Alternatively, brittle shearing in the SASZ and BSZ may represent a discrete tectonic reworking events related to final stage of exhumation of the Neoarchean orogen. The answer remains challenging because a complex structural and temporal relationship, as part of our ongoing research work, exists amongst ductile shear fabric, pseudotachylite emplacement

and brittle shears on mesoscopic scale within the SASZ.

By implication, holistic understanding of tectonic evolution for this ancient orogenic belt remains incomplete without a proper knowledge of timing and duration of ductile to brittle transition in the BSZ and SASZ. Recently, Behera *et al.* (2019) documented a time span of 100 Ma covering last phase of ductile (2.0 Ga) to onset of brittle (1.9 Ga) deformation in the Salem Block. This was followed by a phase of extension and normal faulting at 0.8–0.5 Ga. Lack of comprehensive geochronological record along a representative length of the Neoarchean suture impedes establishing any link for the studied brittle shears with the Pan-African orogenic event. However, in a Pan-African orogenic setup, the SASZ and BSZ seemingly transformed into an intra-cratonic weak zone due to the shift of the active subduction boundary southward, i.e., from MBSASZ to PCSZ (figure 1). In such tectonic scenario, development of mylonitic/phyllonitic fabric and brittle shear bands manifests response of far-field stress. In addition, nature of far-field stress along a paleo-suture zone (BSZ and SASZ together) likely to vary owing to structural and rheological heterogeneities inherited during previous orogenic event. By implication, contrasting tectonic style during brittle shearing event in the BSZ and SASZ, documented in this study, has far-reaching implication on the temporal evolution of the Neoarchean suture zone along the BSZ and SASZ.

## 7. Conclusion

We opine that the study provides new insight on kinematic and tectonic significance of brittle shears, hitherto unexplored, within the SASZ and BSZ. Summarily, important findings of the study include,

- Petrofabric analyses, though limited, provide a first-hand evidence for localized low-T reworking within high-grade charnockite granulites of Salem Block. Detailed petrofabric analyses of phyllonite have significant bearing on dynamics of reworking post-dating the Neoarchean subduction–accretionary tectonics.
- Localizing character for late brittle shears, as evidenced from strain analytical results, manifests a strain softening mechanism, which tallies well with a phase of retrogression and cooling-exhumation of high-grade granulites along the shear zones.
- The studied brittle shear bands may represent a continuum, i.e., late stage phenomenon, of the post-Neoarchean reworking event or a discrete event. However, the available geochronological record specific to this late stage ductile shearing and ductile (mylonite/phyllonite) to brittle transition in the respective shear zone is extremely limited and impedes any regional correlation, in particular, and tectonic correlation in global tectonic framework, i.e., Pan-African Gondwana assembly, in general.
- The contrasting style of brittle shearing, documented in this study, along the two segments (the SASZ and BSZ) of Neoarchean paleo-suture zone possibly underscores interplay between inherited tectonic heterogeneity and later intra-cratonic far-field stress as the dominant mechanism during late-stage reworking.
- Establishing temporal relation between the ductile to brittle transition within and across the BSZ and SASZ may shed important lights on the geodynamics of this ancient orogenic belt and pose a promising future research problem.

## Acknowledgements

AC acknowledges the financial support from Pondicherry University and DST-SERB, Grant-in-Aid No. SERB/F/5928/2018-2019, for carrying out geological fieldwork, sample preparation and analysis. Ritabrata is acknowledged for his support during EBSD analyses. The authors are grateful to the reviewers for their critical suggestions and constructive comments. Prof Saibal Gupta is thanked for editorial handling.

## References

Bhaskar Rao Y J, Chetty T R K, Janardhan A S and Gopalan K 1996 Sm–Nd and Rb–Sr ages and P–T history of the Archaean Sittampundi and Bhavani layered meta-anorthosite complexes in Cauvery Shear zone, south India: Evidence for Neoproterozoic reworking of Archaean crust; *Contrib. Mineral. Petrol.* **125** 237–250.

Bartlett J M, Dougherty-Page J S, Harris N B W, Hawkesworth C J and Santosh M 1998 The application of single zircon evaporation and model Nd ages to the interpretation of polymetamorphic terrains: An example from the Proterozoic mobile belt of south India; *Contrib. Mineral. Petrol.* **131** 181–195.

Beaumont C, Nguyen M H, Jamieson R A and Ellis S 2006 Crustal flow modes in large hot orogens; *Geol. Soc. London, Spec. Publ.* **268** 91–145.

Behera B M, Waele B D, Thirukumaran V, Sundaralingam K, Narayanan S, Sivalingam B and Biswal T K 2019 Kinematics, strain pattern and geochronology of the Salem–Attur shear zone: Tectonic implications for the multiple sheared Salem–Namakkal blocks of the Southern Granulite terrane, India; *Precamb. Res.* **324** 32–61.

Bhadra S and Nasipuri P 2017 Tectonothermal evolution of garnet-bearing quartzo-feldspathic gneiss from the Moyar shear zone, south India: Implications for Neoarchean accretionary tectonics; *Lithos* **274–275** 1–18.

Bhadra B K 2000 Ductile shearing in Attur shear zone and its relation with Moyar shear zone, south India; *Gond. Res.* **3** 361–369.

Bhaskar Rao Y J, Janardhan A S, Vijaya Kumar T, Narayana B L, Dayal A M, Taylor P N and Chetty T R K 2003 Sm–Nd model ages and Rb–Sr isotopic systematics of charnockites and gneisses across the Cauvery Shear Zone, southern India: Implications for the Archean–Neoproterozoic Terrane Boundary in the Southern Granulite Terrain; In: Tectonics of Southern Granulite Terrain: Kuppam–Palani Geotransect (ed.) Ramakrishnan M, *Geol. Soc. India Memoir* **50** 297–317.

Biswal T K, Thirukumaran V, Ratre K, Bandyapadhaya K, Sundaralingam K and Mondal A K 2010 A study of mylonites from parts of the Salem–Attur Shear Zone (Tamil Nadu) and its tectonic implications; *J. Geol. Soc. India* **75** 128–136.

Chetty T R K, Bhaskar Rao Y J and Narayana B L 2003 A structural cross-section along Krishnagiri–Palani Corridor, Southern Granulite Terrain of India; In: Tectonics of Southern Granulite Terrain, Kuppam–Palani Geotransect (ed.) Ramakrishnan M, *Geol. Soc. India* **50** 255–277.

Chetty T R K 1996 Proterozoic shear zones in Southern Granulite Terrain; In: The Archaean and Proterozoic Terrains in Southern India within East Gondwana India (eds) Santos M and Yoshida M, *Gond. Res. Gr. Mem.* **3** 77–89.

Clark C, Collins A S, Timms N E, Kinny P D, Chetty T R K and Santosh M 2009 SHRIMP U–Pb age constraints on magmatism and high-grade metamorphism in the Salem Block, southern India; *Gond. Res.* **16** 27–36.

D'Cruz E, Nair P K R and Prasannakumar V 2000 Palghat gap – a dextral shear zone from the south Indian Granulite Terrain; *Gond. Res.* **3** 21–31.

Dias R and Rebeiro A 1994 Constriction in a transpressive regime: An example in the Iberian branch of the Ibero-Armorican arc; *J. Struct. Geol.* **16** 1543–1554.

Drury S A, Harris N B W, Holt R W, Reeves-Smith G J and Wightman R T 1984 Precambrian tectonics and crustal evolution in southern India; *J. Geol.* **92** 3–20.

Faccenda M, Gerya T V and Chakraborty S 2008 Styles of post-subduction collisional orogeny: Influence of convergence velocity, crustal rheology and radiogenic heat production; *Lithos* **103** 257–287.

Faccenda M and Mancktelow S 2010 Fluid flow during unbending: Implications for slab hydration, intermediate-depth earthquakes and deep fluid subduction; *Tectonophys.* **494** 149–154.

Fletcher J M and Bartley J M 1994 Constrictional strain in a non-coaxial shear zone: Implications for fold and rock fabric development, central Mojave metamorphic core complex, California; *J. Struct. Geol.* **16** 555–570.

Flinn D 1962 On folding during three dimensional progressive deformation; *Quart. J. Geol. Soc.* **118** 385–433.

Fossen H and Tikoff B 1993 The deformation matrix for simultaneous simple shearing, pure shearing and volume change, and its application to transpression–transtension tectonics; *J. Struct. Geol.* **15** 413–422.

Friend C R L and Nutman A P 1991 SHRIMP U–Pb geochronology of the Closepet granite and Peninsular gneisses, Karnataka, south of India; *J. Geol. Soc. India* **38** 357–368.

Ghosh J G, De Wit M J and Zartman R E 2004 Age and tectonic evolution of Neoproterozoic ductile shear zones in the Southern Granulite Terrain of India, with implications for Gondwana studies; *Tectonics* **23** 1–38.

Horsman E and Tikoff B 2007 Constraints on deformation path from finite strain gradients; *J. Struct. Geol.* **29** 256–272.

Hull J 1988 Thickness–displacement relationships for deformation zones; *J. Struct. Geol.* **10** 431–435.

Hunter N J R, Weinberg R F, Wilson C J L and Law R D 2018 A new technique for quantifying symmetry and opening angles in quartz c-axis pole figures: Implications for interpreting the kinematic and thermal properties of rocks; *J. Struct. Geol.* **112** 1–6.

Jain A K, Singh S and Manickavasagam 2003 Intracontinental shear zones in the southern granulite terrane: Their kinematics and evolution; *Geol. Soc. India Memoir* **50** 225–253.

Jiang H, Lee C A, Morgan J K and Ross C H 2015 Geochemistry and thermodynamics of an earthquake: A case study of pseudotachylites within mylonite granitoids; *Earth Planet. Sci. Lett.* **430** 235–248.

Magni V, Faccenna C, Hunen J V and Funiciello F 2013 Delamiantion *vs.* break-off: The fate of continental collision; *Geophys. Res. Lett.* **40** 285–289.

Means W D 1984 Shear zones of types I and II and their significance for reconstruction of rock history; *Geol. Soc. Am. Abs.* **16** 50.

Means W D 1995 Shear zones and rock history; *Tectonophys.* **247** 157–160.

Meiβner B, Deters P, Srikantappa C and Köhler H 2002 Geochronological evolution of the Moyar, Bhavani and Palghat shear zones of southern India: Implications for east Gondwana correlations; *Precamb. Res.* **114** 149–175.

Mukhopadhyay D, Kumar S P, Srinivasan R and Bhattacharya T 2003 Nature of the Palghat–Cauvery lineament in the region south of Namakkal, Tamil Nadu: Implications for terrane assembly in the south Indian granulite province; In: *Tectonics of Southern Granulite Terrain, Kuppam–Palani Geotransect* (ed.) Ramakrishnan M, *Geol. Soc. India Memoir* **50** 279–296.

Naha K and Srinivasan R 1996 Nature of Moyar and Bhavani shear zone with a note on its implication on the tectonics of the southern Indian peninsula shield; *Proc. Acad. Sci. (Earth Planet. Sci.)* **105** 173–189.

Nair P K R, Prasannakumar V and Thomas M 1981 Structure of the western termination of the Bhavani lineament; *J. Geol. Soc. India* **22** 285–291.

Neumann B 2000 Texture development of recrystallised quartz polycrystals unraveled by orientation and misorientation characteristics; *J. Struct. Geol.* **22** 1695–1711.

Passchier W 1984 The generation of ductile and brittle shear bands in a low-angle mylonite zone; *J. Struct. Geol.* **6** 273–281.

Peucat J J, Mahabaleswar B and Jayananda M 1993 Age of younger tonalitic magmatism and granulite metamorphism in the South Indian transition zone (Krishnagiri area): Comparison with older Precambrian gneisses from Hassan–Gorur area; *J. Metamorph. Geol.* **11** 879–888.

Prasannakumar V and McCaig A 2016 Reactivation and strain localisation in Bhavani Shear Zone, South India; *J. Geol. Soc. India* **88** 421–432.

Prasannakumar V and Lloyd G E 2007 Development of crystallographic lattice preferred orientation and seismic properties in Bhavani shear zone, southern India; *J. Geol. Soc. India* **70** 282–296.

Prasannakumar V and Lloyd G E 2010 Application of SEMEBSD to regional scale shear zone analysis: A case study of the Bhavani shear zone, south India; *J. Geol. Soc. India* **75** 183–201.

Pratheesh P, Prasannakumar V and Praveen K R 2013 Magnetic fabrics in characterization of magma emplacement and tectonic evolution of the Moyar Shear Zone, south India; *Geosci. Front.* **4** 113–122.

Raith M, Srikantappa C, Buhl D and Koehler H 1999 The Nilgiri enderbites, south India: Nature and age constraints on protolith formation, high grade metamorphism and cooling history; *Precamb. Res.* **98** 129–150.

Ramakrishnan M 2003 Craton-mobile belt relations in Southern Granulite Terrain; In: *Tectonics of Southern Granulite Terrain, Kuppam–Palani Geotransect* (ed.) Ramakrishnan M, *Geol. Soc. India Memoir* **50** 1–24.

Ramsay J G 1967 *Folding and Fracturing of the rocks*; McGraw Hill, New York, 568p.

Ramsay J G 1980 Shear zone geometry: A review; *J. Struct. Geol.* **2** 83–99.

Ratheesh-Kumar R T, Santosh M, Yang Q Y, Ishwar-Kumar C, Chen N S and Sajeev K 2016 Archean tectonics and crustal evolution of the Biligiri Rangan Block, southern India; *Precamb. Res.* **275** 406–428.

Santosh M and Sajeev K 2006 Anticlockwise evolution of ultrahigh-temperature granulites within the continental collision zone in southern India; *Lithos* **92** 447–464.

Santosh M, Maruyama S and Sato K 2009 Anatomy of a Cambrian suture in Gondwana: pacific-type orogeny in southern India; *Gond. Res* **16** 321–341.

Satheeshkumar R and Prasannakumar V 2009 Fabric evolution in Salem–Attur shear zone, south India and its implications on the kinematics; *Gond. Res.* **16** 37–44.

Sato K, Santosh M, Tsunogae T, Chetty T R K and Hirata T 2011 Laser ablation ICP mass spectrometry for zircon U–Pb geochronology of metamorphosed granite from the Salem Block: Implication for Neoarchean crustal evolution in southern India; *J. Min. Petrol. Sci.* **106** 1–12.

Sawant A D, Gupta S, Clark C and Misra S 2017 The Rauer–Rengali connection in the Indo-Antarctica amalgam: Evidence from structure, metamorphism and geochronology; *Geol. Soc. London, Spec. Publ.* **457** 171.

Sorcar N, Hoppe U, Dasgupta S and Chakraborty S 2014 High-temperature cooling histories of migmatites from the High Himalayan Crystallines in Sikkim, India: Rapid cooling unrelated to exhumation; *Contrib. Mineral. Petrol.* **167** 957.

Sundaralingam K, Biswal T K and Thirukumaran V 2017 Strain analysis of the Salem–Attur shear zone of Southern Granulite Terrane around Salem, Tamil Nadu; *J. Geol. Soc. India* **89** 5–11.

Tikoff B and Fossen H 1993 Simultaneous pure and simple shear: The unified deformation matrix; *Tectonophys.* **217** 267–283.

Vitale S and Mazzoli S 2016 From finite to incremental strain: Insights into heterogeneous shear zone evolution; In: *Ductile shear zones from micro- to macro-scales* (eds) Mukherjee S and Mulchrone K F, John Wiley & Sons, USA, 306p.

Vitale S and Mazzoli S 2008 Heterogeneous shear zone evolution: The role of shear strain hardening/softening; *J. Struct. Geol.* **30** 1363–1395.

Vitale S and Mazzoli S 2009 Finite strain analysis of a natural ductile shear zone in limestones: Insights into 3-D coaxial vs. non-coaxial deformation partitioning; *J. Struc. Geol.* **31** 104–113.

Vitale S and Mazzoli S 2010 Strain analysis of heterogeneous ductile shear zones based on planar markers; *J. Struct. Geol.* **32** 321–329.

Corresponding editor: Saibal Gupta